Digest Journal of Nanomaterials and Biostructures

Dig. J. Nanomater. Bios. **2026**; 21(3): 53220
https://doi.org/10.31083/DJNB53220

Original Research

Structure-Property Correlation in TiO_2-CdS/Zeolite Hybrid Composites: Influence of Natural and Synthetic Supports on Lattice Strain and Photocatalytic Behavior

Hugo Armando de la Cruz Hernández[1], Erik Ramírez Morales[1], Lizeth Rojas Blanco[1], Maria Guadalupe Hernández Cruz[2], Fanny Servín de Dios[3], Marcela del Carmen Arellano Cortaza[1,*]

[1]División Académica de Ingeniería y Arquitectura, Universidad Juárez Autónoma de Tabasco, 86040 Villahermosa, Mexico
[2]División Académica Multidisciplinaria de Jalpa de Méndez, Universidad Juárez Autónoma de Tabasco, 86040 Villahermosa, Mexico
[3]Área Académica de Ciencias de la Tierra y Materiales, Universidad Autónoma del Estado de Hidalgo, 42184 Hidalgo, Mexico
*Correspondence: marcela.arellano@ujat.mx (Marcela del Carmen Arellano Cortaza)
Academic Editor: Shaik Gouse Peera
Submitted: 23 April 2026 Revised: 29 May 2026 Accepted: 5 June 2026 Published: 8 September 2026

Abstract

Background: The development of advanced materials catalyzing solar-driven degradation is essential for sustainable water remediation strategies. This study sheds light on how zeolitic supports influence the microstructural and charge-transfer properties of ternary photocatalysts. **Methods:** Hybrid Titanium dioxide (TiO_2)-cadmium sulfide (CdS) composites supported on natural (clinoptilolite) and synthetic (NaA) zeolites were synthesized via an *in situ* sol–gel method. The structural and optical properties of these composites were characterized using instrumental techniques, and their photocatalytic performance was evaluated through the degradation of methylene blue (MB) under simulated solar light. **Results:** X-ray diffraction identified anatase as the dominant phase. Williamson-Hall analysis revealed a reduction in TiO_2 crystal size (from 7.2 nm for bare TiO_2 to 5.6 nm for the optimal composite) and support-dependent compressive lattice deformation. Specific surface area increased (from 65.88 to 78.91 m^2/g) with the emergence of hierarchical porosity. The TiO_2-CdS/clinoptilolite composite with a moderate zeolite content (TiO_2-CdS/CLI0.5) exhibited the most balanced performance, featuring an optimal crystallite size, a moderate compressive lattice strain, a low recombination rate, and an absolute photocatalytic MB degradation of 53% (as well as 16% dark adsorption), outperforming synthetic NaA counterparts. **Conclusions:** The zeolitic support strongly influences structure–property relationships in TiO_2-CdS/zeolite composites. By acting as rigid nanoreactors, the matrices induce microstrain and facilitate charge separation via a direct Z-scheme mechanism, thereby enhancing visible-light photocatalysis.

Keywords: TiO_2-CdS; zeolites; methylene blue; photocatalysis

1. Introduction

Water contamination by persistent organic pollutants remains one of the most pressing environmental challenges, as industrial effluents frequently contain dyes and recalcitrant composites that are difficult to remove using conventional physicochemical or biological treatments [1,2]. Among these contaminants, synthetic dyes such as methylene blue (MB) exhibit high chemical stability, resistance to biodegradation, and strong light absorption, which limits solar penetration in aquatic systems and disrupts ecological balance [3,4]. Consequently, the development of advanced materials capable not only of adsorption but also of catalytic degradation is essential for sustainable water remediation strategies.

Heterogeneous photocatalysis has emerged as a promising approach due to its ability to mineralize organic pollutants under light irradiation [5]. Titanium dioxide (TiO_2), particularly in its anatase phase, is one of the most widely investigated photocatalysts owing to its chemical stability, low toxicity, and strong oxidative capacity. However, its wide band gap (~3.2 eV) restricts photoactivation predominantly to the ultraviolet region, limiting solar energy utilization [5]. To overcome this limitation, narrow-band-gap semiconductors such as cadmium sulfide (CdS, ~2.4 eV) have been coupled with TiO_2 to extend light absorption into the visible range. The formation of TiO_2-CdS composites enhances charge separation efficiency and broadens the spectral response. In fact, advanced interfacial designs utilizing CdS, such as S-scheme heterojunctions, have recently been shown to highly optimize reaction kinetics and directed charge-transfer pathways for enhanced photocatalytic performance [6]. Despite these mechanistic advantages, challenges related to the photocorrosion and long-term structural instability of CdS in aqueous media remain [5].

Beyond band gap engineering, the structural design of composite materials plays a crucial role in determining their functional performance. The deliberate design of hybrid interfaces has been shown to significantly enhance material properties by optimizing physical and chemical interactions

at the interface [7]. In multiphase photocatalytic systems, these interfacial interactions between semiconductors and supports become even more critical; they can induce lattice distortions, modify defect densities, and create synergistic effects at the heterojunctions. Such synergistic enhancement strongly dictates charge-carrier dynamics, ultimately leading to highly efficient and recoverable dye degradation under visible light [8].

In this context, porous aluminosilicate frameworks, such as zeolites, have attracted attention as functional supports due to their high surface area, tunable pore structures, and ion-exchange capacity [5]. Zeolites not only improve dispersion and inhibit nanoparticle aggregation but also modulate adsorption behavior and facilitate interfacial bonding (e.g., Ti-O-Si linkages), thereby impacting crystallite growth and strain within semiconductor phases.

Recent studies have highlighted the potential of zeolite-supported TiO_2 systems for enhanced environmental applications [5]. However, limited attention has been paid to how the topology and ionic composition of natural versus synthetic zeolites influence the structural parameters of TiO_2-CdS composites, including crystallite size, lattice strain, and defect-related recombination processes. In particular, clinoptilolite (rich in exchangeable cations such as Ca^{2+}, K^+, and Mg^{2+}) and NaA-type zeolite (dominated by Na^+ ions and smaller pore apertures) provide distinct physicochemical environments that may significantly affect composite formation and structure–property relationships.

Therefore, the present study focuses on the synthesis of TiO_2-CdS/zeolite hybrid composites via the sol-gel method, employing both natural (clinoptilolite) and synthetic (NaA) zeolites as supports. While numerous studies have explored TiO_2-CdS heterostructures, the novelty of this work lies in the *in situ* sol-gel synthesis method, which systematically correlates how the different topological and ionic environments of NaA zeolites determine structural microdeformation and charge-carrier dynamics. This study directly compares how these specific zeolitic structures, which differ in pore opening and exchangeable cations, physically restrict TiO_2 crystal growth and modulate interfacial defects. Through this sol-gel strategy, we elucidate the fundamental mechanisms by which zeolitic support enhances photocatalytic efficiency under visible light, beyond traditional band-gap reduction.

2. Materials and Methods

2.1 Chemicals and Materials

Titanium tetrabutoxide ($Ti[OC(CH_3)_3]_4$, Sigma Aldrich, St. Louis, USA, 97%), anhydrous ethanol (C_2H_6O, JT Baker, New Jersey, USA), hydrochloric acid (HCl, Sigma Aldrich, St. Louis, USA), cadmium acetate ($(CH_3COO)_2Cd{\cdot}2H_2O$, Sigma Aldrich, St. Louis, USA, 99%), sodium sulfide ($Na_2S{\cdot}9H_2O$, Sigma Aldrich, St. Louis, USA, 98%), and deionized water were utilized for material synthesis. The natural zeolite used was calcium clinoptilolite from El Cajón, Sonora, Mexico, sieved through #360 mesh, and type A sodium zeolite was used as the synthetic zeolite (Sigma-Aldrich, St. Louis, USA). Analytical grade MB ($C_{16}H_{18}ClN_3S$, JT Baker, New Jersey, USA) served as the model contaminant.

2.2 Synthesis of TiO_2

A solution containing 25 mL of C_2H_6O and 13 mL of $Ti[OC(CH_3)_3]_4$ was maintained under magnetic stirring for 30 minutes. Subsequently, 1 mL of HCl was added as a catalyst. Separately, a solution of 10 mL of C_2H_6O and 2.7 mL of deionized water was prepared and added dropwise to the $Ti[OC(CH_3)_3]_4$ mixture. The titration process required approximately 20 minutes under constant magnetic stirring. The resulting solution was stirred for an additional 20 hours. The mixture was then dried in a water bath at 90–100 °C until a white powder formed, which was ground using an agate mortar. The material was heat-treated in a tubular furnace at 500 °C under an oxygen flow for 1 hour. The final sample was labeled as TiO_2.

2.3 Synthesis of CdS

CdS was obtained using the sol-gel method, based on the methodology of Manzoor et al. [9]. A 0.5 M $(CH_3COO)_2Cd{\cdot}2H_2O$ solution was prepared in 100 mL of deionized water, stirred for 30 minutes, and then subjected to static aging for another 30 minutes. The resulting product was recovered by centrifugation and then washed repeatedly with deionized water and ethanol. This material was then dried at 90 °C in a water bath to facilitate the removal of residual solvent and finally ground into a fine powder for subsequent use.

2.4 Synthesis of TiO_2-CdS/Zeolite Composites

The synthesis of the TiO_2-CdS/Zeolite composites was carried out similarly to the methodology used for the preparation of TiO_2. The incorporation of zeolite and CdS was carried out by adding 0.074 g of CdS (previously synthesized) and different amounts of zeolite (0.5 g and 1.5 g) during the preparation of the sol phase. The rest of the process is similar to that previously described for the synthesis of TiO_2. The samples were labeled TiO_2-CdS/CLI0.5, TiO_2-CdS/CLI1.5, TiO_2-CdS/NaA0.5, and TiO_2-CdS/NaA1.5 for the composites with 0.5 g and 1.5 g of natural (CLI) and synthetic (NaA) zeolites, respectively.

2.5 Characterizations and Equipment

The structural characterization of the samples was performed using X-ray diffraction and Raman spectroscopy. A Bruker D2 Phaser (Billerica, Massachusetts, USA) diffractometer was used, emitting Cu Kα radiation (λ = 1.5406 Å). Diffractions were recorded in the 2θ range of 10–80° at a scan rate of $4°{\cdot}min^{-1}$ under standard equipment conditions. Raman analysis was performed on a Horiba–Jobin

iHR550 spectrometer (Horiba, Kyoto, Japan) using a 533 nm (green) laser excitation source at room temperature. Optical analysis was performed using Ultraviolet-Visible (UV)-Visible spectroscopy (SHIMADZU UV-2600, Kyoto, Japan) and photoluminescence (PL) spectroscopy (λ = 533 nm; Horiba-Jobin iHR550 monochromator (Kyoto, Japan) and a Peltier-cooled Synapse CCD detector with a collection lens system for emission capture). Textural analyses were performed by nitrogen (N_2) physisorption on an Autosorb iQ (Anton Paar, Graz, Austria). Before measurement, the powdered samples were degassed at 200 °C (473.15 K) under vacuum to remove moisture and physisorbed species, ensuring clean surfaces. N_2 adsorption-desorption isotherms were recorded at 77 K (−196.15 °C) using a liquid nitrogen bath.

The photocatalytic tests were performed using a fully reflective Sciencetech solar simulator (London, Ontario, Canada) that employs a 500 W xenon short-arc lamp as the irradiation source, which was calibrated to deliver a light intensity of 1 sun (approximately 100 mW/cm^2) at the sample surface. The reaction was monitored using a UV-Vis spectrophotometer with the main MB band located at 665 nm. The photocatalytic tests were designed as proof-of-concept evaluations to assess the baseline visible-light activity of the composites.

3. Results

3.1 X-Ray Diffraction (XRD)

X-ray diffraction was used to determine the crystalline structure of the composites synthesized with varying zeolite percentages. Fig. 1 shows the diffractograms of the sol-gel-synthesized samples. The data were compared with the JCPDS 21-1272 card. All samples exhibit peaks that can be indexed to the anatase phase of TiO_2 (tetragonal structure), which has three principal planes (101), (200), and (004) located at approximately 2θ: 25°, 38°, and 48°, respectively [10].

Fig. 1a shows the composites synthesized with natural zeolite. These samples were compared with the JCPDS 39-1383 card. In the TiO_2-CdS/CLI1.5 sample, a greater number of peaks corresponding to clinoptilolite- Ca [11] can be distinguished than in the TiO_2-CdS/CLI0.5 sample, which is associated with the amount of zeolite incorporated in the synthesis process, since a higher mass percentage of zeolite results in more crystal planes that can diffract the X-ray beam [12]. A similar phenomenon is observed in the samples made with synthetic zeolite. In the TiO_2-CdS/NaA0.5 sample, it is not possible to distinguish any peak associated with the sodium zeolite, while the TiO_2-CdS/NaA1.5 sample exhibits the planes (642), (660), (1200), and (1088), located at 2θ: 27°, 32°, 45°, and 56°, respectively [13].

In none of the samples were peaks corresponding to CdS in the cubic zinc blende phase observed, due to the amount of precursor salt used in the synthesis. Furthermore, the (200) plane of CdS overlaps with the (101) plane of TiO_2, complicating indexing. However, the TiO_2 planes exhibit shifts to the right and left, as well as broadening, as shown in Fig. 1c. This behavior in the diffractograms indicates that the CdS particles generate strain in the TiO_2 lattice. Although the low precursor concentration and the critical overlap between the CdS (200) and TiO_2 (101) planes limit the direct detection of the CdS phase via XRD, its successful incorporation and dispersion are unequivocally confirmed by complementary spectroscopic analyses discussed in the following sections.

The Williamson-Hall uniform deformation model (UDM) was employed to estimate lattice deformation in TiO_2 resulting from the incorporation of CdS particles and the application of zeolites as supports. The UDM model considers [14]:

$$\beta \cos\theta = \frac{K\lambda}{D} + 4\varepsilon \sin\theta. \quad (1)$$

where K is a shape factor (0.9), and ε is the microstrain. From a linear fit of the graph of $\beta \cos\theta$ vs 4 $\sin\theta$ for the diffraction peaks, we can determine the slope and intercept on the ordinate axis, representing the strain and crystallite size, respectively [15] (Fig. 2a). The data obtained are summarized in Table 1.

Table 1 shows that the compressive lattice strain of TiO_2 increases with higher proportions of CdS and zeolites, particularly in the TiO_2-CdS/CLI1.5 and TiO_2-CdS/NaA1.5 composites. In contrast, the microstrain slightly relaxes for the 0.5 composites compared to bare TiO_2. These structural perturbations alter the “a” and “c” lattice parameters due to the incorporation of cadmium ions. The presence of Cd and S atoms causes structural imbalances in TiO_2, as titanium ions can be replaced by cadmium ions, or these new ions may occupy interstitial spaces [16,17], resulting in modifications to the lattice parameters (Fig. 2c). Some reports suggest that the incorporation of Cd species into TiO_2 can generate local lattice distortions due to ionic size mismatch and possible substitutional or interstitial incorporation [18].

These structural perturbations may lead to uniform lattice deformation, modifying the lattice parameters and inducing strain within the anatase structure. Such distortion effects are consistent with the shifts observed in the diffraction peaks and the strain values obtained from Williamson-Hall analysis.

When the zeolite amount decreases in composites (TiO_2-CdS/CLI1.5 and TiO_2-CdS/NaA1.5), the TiO_2 diffraction peak intensity also drops, which may be associated with possible Ti-O-Si interfacial interactions, as suggested by similar supported systems [19].

Negative lattice strain values in Table 1 indicate compressive forces [17]. These forces stem from two effects: localized lattice distortions due to the ionic radius mismatch between Cd or S species and TiO_2. It is well established that substitution or interstitial placement of ions with differing

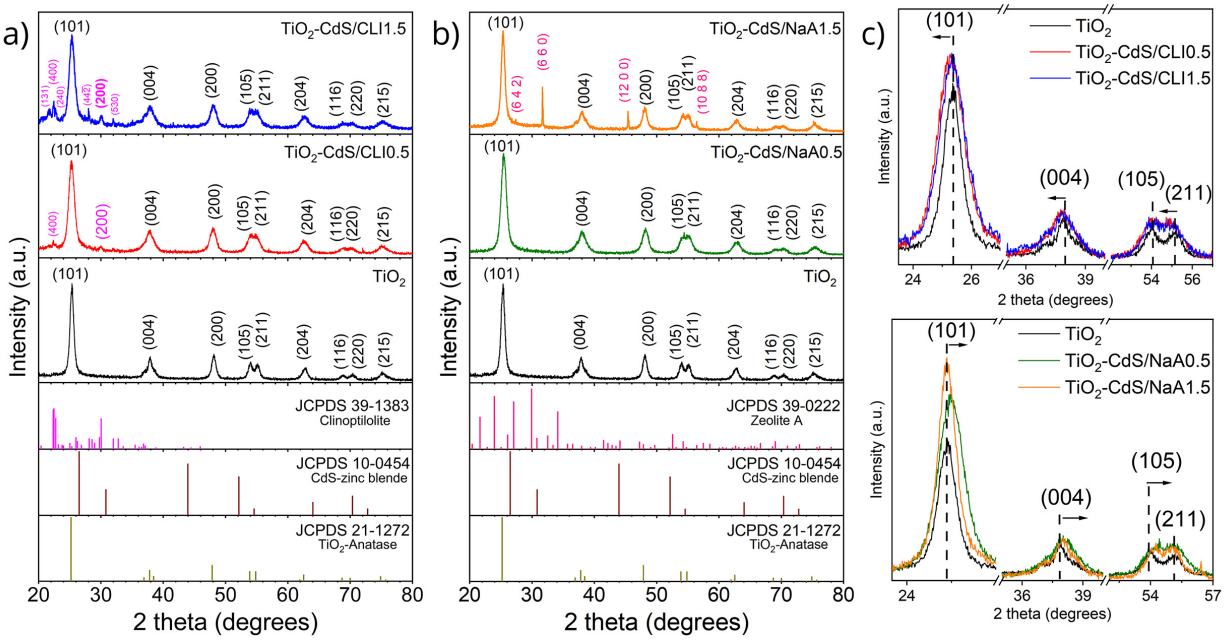

Fig. 1. X-ray diffraction patterns of the composites with different percentages of zeolites: (a) TiO_2-CdS/CLI and (b) TiO_2-CdS/NaA. (c) Magnified view highlighting the shift and broadening of the TiO_2 diffraction peaks. TiO_2, Titanium dioxide; CdS, cadmium sulfide.

Table 1. Structural parameters estimated by X-ray diffraction (XRD) of TiO_2 particles synthesized with different percentages of zeolites, natural and synthetic.

Sample	Average crystallite size (nm)	Strain (slope)	R^2	Lattice parameters (Å)	
				a	c
TiO_2	7.2	–0.00434 ± 0.00208	0.49	3.7870	9.5109
TiO_2-CdS/CLI0.5	5.6	–0.00401 ± 0.00225	0.51	3.7963	9.5338
TiO_2-CdS/CLI1.5	4.6	–0.00772 ± 0.00305	0.75	3.7934	9.5341
TiO_2-CdS/NaA0.5	6.0	–0.00262 ± 0.00251	0.21	3.7811	9.4756
TiO_2-CdS/NaA1.5	6.5	–0.00520 ± 0.00305	0.54	3.7892	9.4848

ionic radii forces the host unit cell to locally deform, thereby generating microstrain [18,20]. Physical confinement by rigid zeolitic pores acts as nanoreactors, which restrict TiO_2 crystallite expansion during thermal treatment. This spatial constraint, discussed in zeolite catalysis studies, prevents complete structural relaxation and results in residual compressive stress upon cooling [21]. To assess the reliability of the UDM, a statistical error analysis was performed (Table 1). The linear fits show moderate-to-low R^2 values and data scatter, a known UDM limitation reflecting the anisotropic anatase tetragonal lattice, where strain isn't uniform in all directions. Despite this, standard errors confirm the trend: CdS and zeolitic supports induce net compressive microstrain in TiO_2 compared to the bare material. In Fig. 2b, TiO_2 crystallite size generally decreased with the incorporation of the zeolites, since these inhibit the aggregation and growth of TiO_2, ensuring that the semiconductor particles are dispersed in the support [22,23], in addition to the fact that the pores of the zeolites act as micro-reactors, which restrict the growth of TiO_2 [24].

It is worth noting that the incorporation of the zeolitic matrix from the initial synthesis stages is fundamentally required to prevent the severe nanoparticle agglomeration typically observed in bare TiO_2-CdS binary systems. By acting as rigid structural templates, the zeolites ensure high nanometric dispersion and protect the active phases, which is why the ternary composites are evaluated against the fundamental bare TiO_2 benchmark rather than a highly aggregated binary control.

3.2 Raman Spectroscopy

According to group theory, the tetragonal structure of TiO2 (space group I4/amd D_{4h}^{19}) has 15 optical modes [25]:

$$\Gamma = A_{1g} + A_{2u} + 2B_{1g} + B_{2u} + 3E_g + 2E_u. \quad (2)$$

Since, A_{1g}, B_{1g} and E_g are Raman-active, six signals would be expected in the anatase phase spectrum.

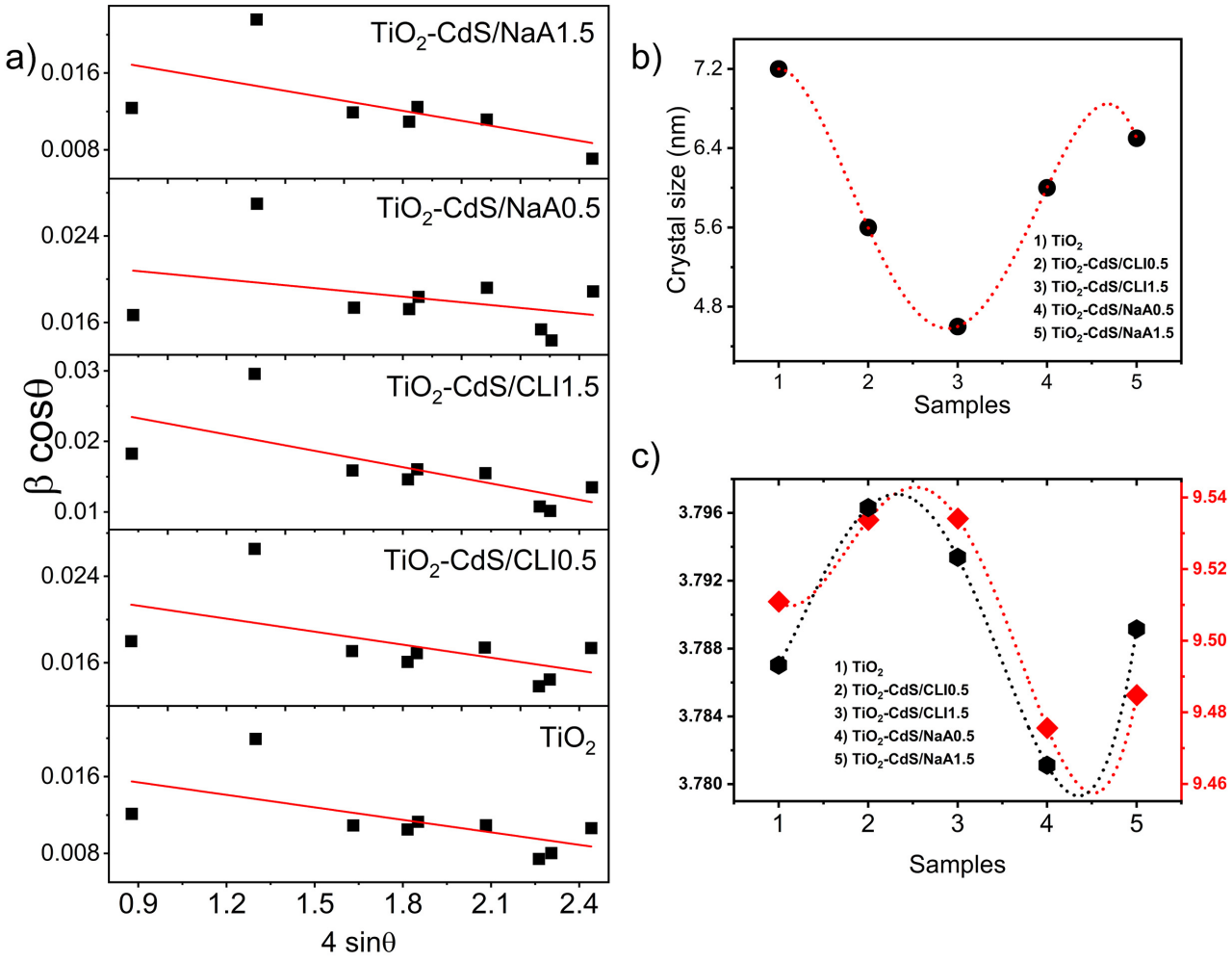

Fig. 2. Structural parameters of the synthesized materials. (a) W-H analysis of TiO_2 particles using the uniform deformation model (UDM). Linear fit of the data; strain is extracted from the slope, and crystallite size is obtained using the y-intercept. (b) Crystal size and (c) lattice parameters of the tetragonal structure of the anatase phase.

The TiO_2, TiO_2-CdS/CLI0.5, and TiO_2-CdS/NaA0.5 samples were structurally analyzed by Raman spectroscopy; the spectra are presented in Fig. 3. All the analyzed samples exhibit characteristic signals of the anatase phase. The signals located at ~144 cm^{-1} (E_{g1}) and 197 cm^{-1} (E_{g2}) are associated with the symmetric vibrational mode of the O-Ti-O bond stretching [26]. At 395 cm^{-1} (B_{1g}), a signal associated with the symmetric bending of these same bonds is observed [27].

The signal located at ~514 cm^{-1} is composed of the A_{1g} and B_{1g} modes, which are associated with antisymmetric and symmetric bending, respectively, of the Ti-O-Ti [28]. Finally, the signal at ~640 cm^{-1} (E_{g3}) confirms the anatase structure in the synthesized samples.

We observe that these signals exhibit intensity changes and blue shifts in the samples containing CdS and zeolites. The changes in intensity can be attributed to the scattering of TiO_2 particles within the zeolite matrix, the inhibition of TiO_2 crystal growth, and the formation of Si-O-Si bonds [24,29].

On the other hand, the shifts to higher wavenumbers corroborate the strains generated in the TiO_2 lattice by the CdS particles, due to the difference between the lattice parameters of these two materials, as well as the possible substitutions of Cd^{2+} with Ti^{4+} or the interstitial arrangement of Cd^{2+} in the anatase structure. Furthermore, these shifts are associated with a decrease in TiO_2 crystal size in the synthesized composites [27]. In addition to the characteristic signals of the anatase phase, two additional signals were observed for the pure TiO_2 sample, located at 280 and 585 cm^{-1}. These signals have been reported as structural disorders. The disappearance of both signals in the composites confirms that the zeolites and CdS particles cause the TiO_2 crystals to shrink and promote their ordered growth [16].

3.3 UV-Vis Spectroscopy and Photoluminescence (PL)

Fig. 4a shows the absorption spectrum for TiO_2 particles and composites synthesized with different percentages of zeolites. All samples exhibit an intense absorption edge in the UV region (200–400 nm), typical of the anatase phase

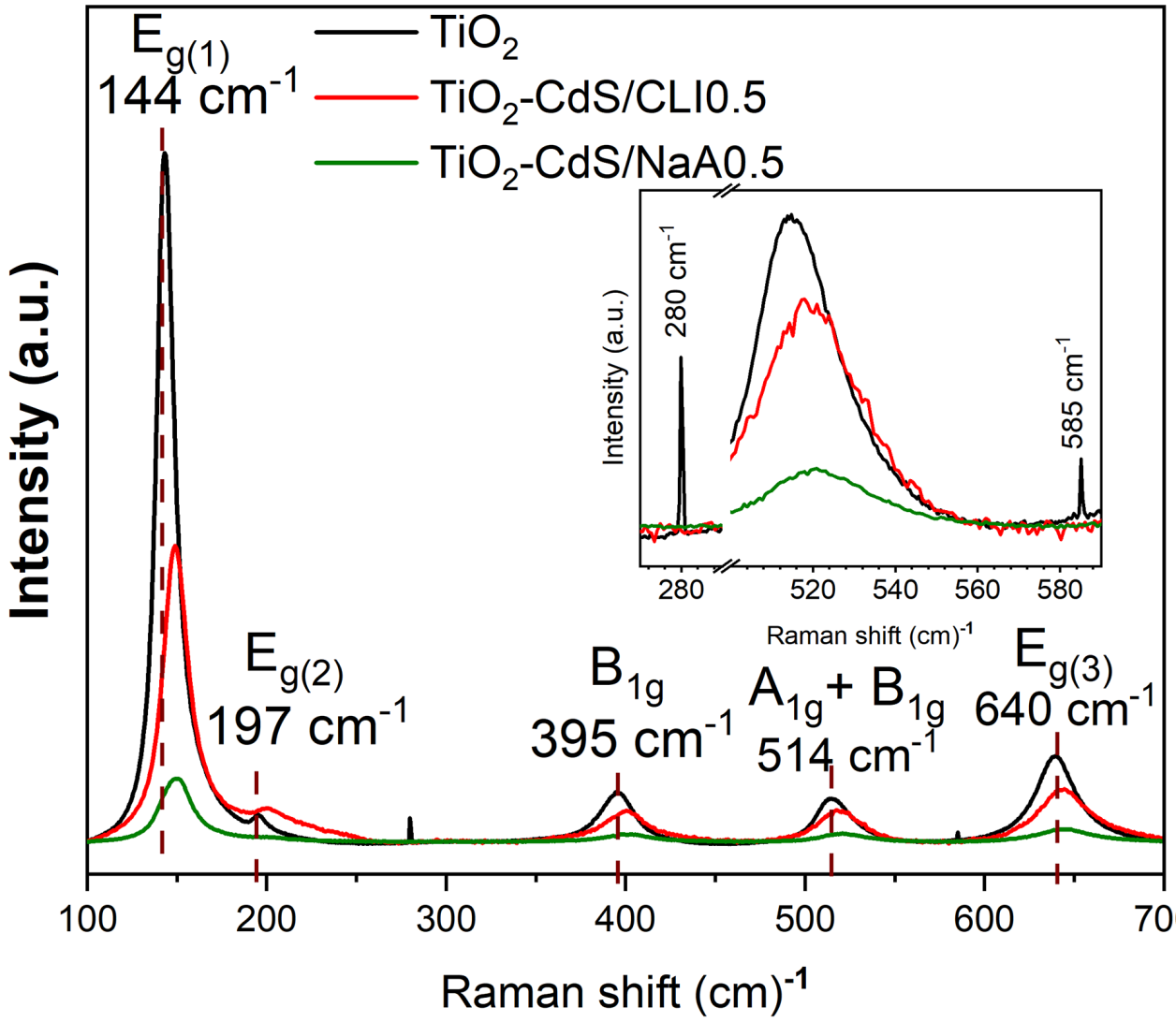

Fig. 3. Raman spectra at room temperature of TiO_2 particles and sol-gel synthesized composites.

of the material [30]. In the synthesized composites, absorption in the UV region increased due to the presence of zeolites, which absorb only in this region of the spectrum, ~250 nm [31].

It can be observed that all composites, except for TiO_2-CdS/NaA0.5, exhibited an increase in absorbance in the visible region compared to pure TiO_2. This can be attributed to the CdS particles, whose absorption boundary extends from 400 nm to 600 nm [32].

The energy gap (E_g) value for each sample was determined by extrapolating from the Kubelka-Munk plots $(F(R) \cdot h\nu)^{\frac{1}{2}}\ \nu s h\nu$ (inset Fig. 4a). The energy gap values were in the following order: TiO_2 (3.21 eV) < TiO_2-CdS/CLI1.5 (3.24 eV) < TiO_2-CdS/NaA0.5 (3.25 eV) < TiO_2-CdS/CLI0.5 (3.26 eV) < TiO_2-CdS/NaA1.5 (3.28 eV). Although CdS has a narrower band gap (~2.4 eV), the slight increase in the estimated band gap values of the composites compared to pure TiO_2 can be attributed to two main factors. First, the reduction in the size of the TiO_2 crystals, as determined by X-ray diffraction (XRD), may induce quantum confinement effects, leading to a slight increase in the band gap. Second, Tauc analysis indicates that the anatase phase of TiO_2; therefore, the improvement in visible light activity is not directly associated with a decrease in the band gap, but rather with better interfacial charge separation between TiO_2 and CdS, as corroborated by the photoluminescence results. As evidenced by our Williamson-Hall analysis, the incorporation of CdS induces a compressive microstrain in the TiO_2 lattice. Recent fundamental studies have demonstrated that such strain-induced structural distortion promotes charge delocalization and achieves ultralow exciton binding energies, thereby providing a strong driving force for spatial charge separation [33]. Consequently, this strain-driven mechanism, alongside the formation of the heterojunction, facilitates the transfer of electrons from CdS to TiO_2, which

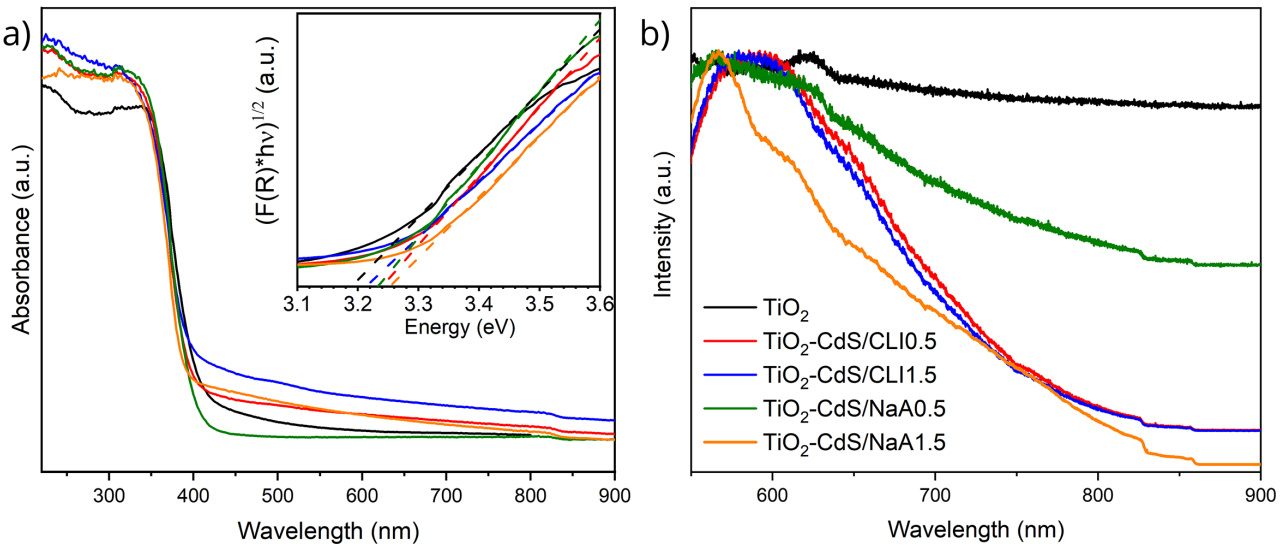

Fig. 4. Optical properties of the synthesized materials. (a) Ultraviolet-Visible (UV)-Vis absorption spectra of the TiO_2 and TiO_2-CdS/Zeolite composite samples. Inset: Tauc plot of the samples with indirect transitions. (b) Photoluminescence (PL) spectra recorded at room temperature with excitation at 533 nm.

reduces recombination and promotes photocatalytic efficiency despite the slight increase in apparent bandwidth values.

Fig. 4b presents the photoluminescence spectra. It is important to note that a 533 nm (sub-bandgap) excitation source was deliberately utilized for the PL measurements. While intrinsic band-to-band excitation of pure TiO_2 requires UV irradiation, sub-bandgap excitation allows specific probing of deep trap states, such as oxygen vacancies, and evaluates the recombination dynamics associated exclusively with the visible-light response induced by the CdS heterojunction [34]. Under this visible excitation, the pure TiO_2 sample displays a defect-related band at approximately 621 nm, which is fundamentally attributed to the recombination of excitons trapped in oxygen vacancies [35].

In the composites, the PL signal intensity is significantly quenched. PL emission directly indicates the radiative recombination of photogenerated electron-hole pairs, so this pronounced reduction shows a strongly suppressed recombination rate. The proposed direct Z-scheme mechanism effectively separates charges at the interface, prolonging charge-carrier lifetime. As a result, more highly reactive electrons and holes survive and migrate to the catalyst surface. This process links quenched PL intensity with the enhanced photocatalytic performance of the composites (particularly TiO_2-CdS/CLI0.5), as more separated charges drive the generation of reactive oxygen species ($O_2^{\cdot-}$ and $OH\cdot$) required for dye mineralization [36,37,38]. Additionally, the composites display a band near 565 nm, which is linked to sulfur vacancies or surface defects in CdS. The observed blue shifts in the composites are likely related to the interface ratio between CdS and TiO_2 particles [39,40].

3.4 N_2 Physisorption

The N_2 adsorption-desorption isotherms and the corresponding BJH pore-size distribution curves for all synthesized materials are shown in Fig. 5.

Specific surface area was estimated using the Brunauer–Emmett–Teller (BET) multipoint method. According to the International Union of Pure and Applied Chemistry (IUPAC) classification, all samples exhibit type IV adsorption isotherms with a hysteresis loop H3 [41]. These characteristics reveal the hierarchical nature of the zeolites used as supports; that is, they combine the nature of micro- and mesopores [42], which are beneficial in photocatalytic tests because they increase the contact surface with contaminants, thus promoting their removal. As observed in the Barrett–Joyner–Halenda (BJH) plots (Fig. 5, insets a–e), all samples exhibit a monomodal distribution centered at 5 nm.

Overall, the composites demonstrated an increase in specific surface area, ranging from 78.91 to 98.60 m^2/g, and a decrease in pore size by approximately 27 to 31 percent compared to pure TiO_2. In contrast, the TiO_2-CdS/NaA1.5 composite demonstrated a 13.7 percent decrease in specific surface area (56.83 m^2/g) and a 12.5 percent reduction in pore size. This behavior may be related to the microporous nature of the zeolites and/or the collapse of large pores due to the heat treatment of the samples or the incorporation of the TiO_2-CdS particles into the porous structure of the zeolites, as shown in Fig. 5f. This composite arrangement prevents TiO_2 particles from agglomerating during photocatalysis in the aqueous system.

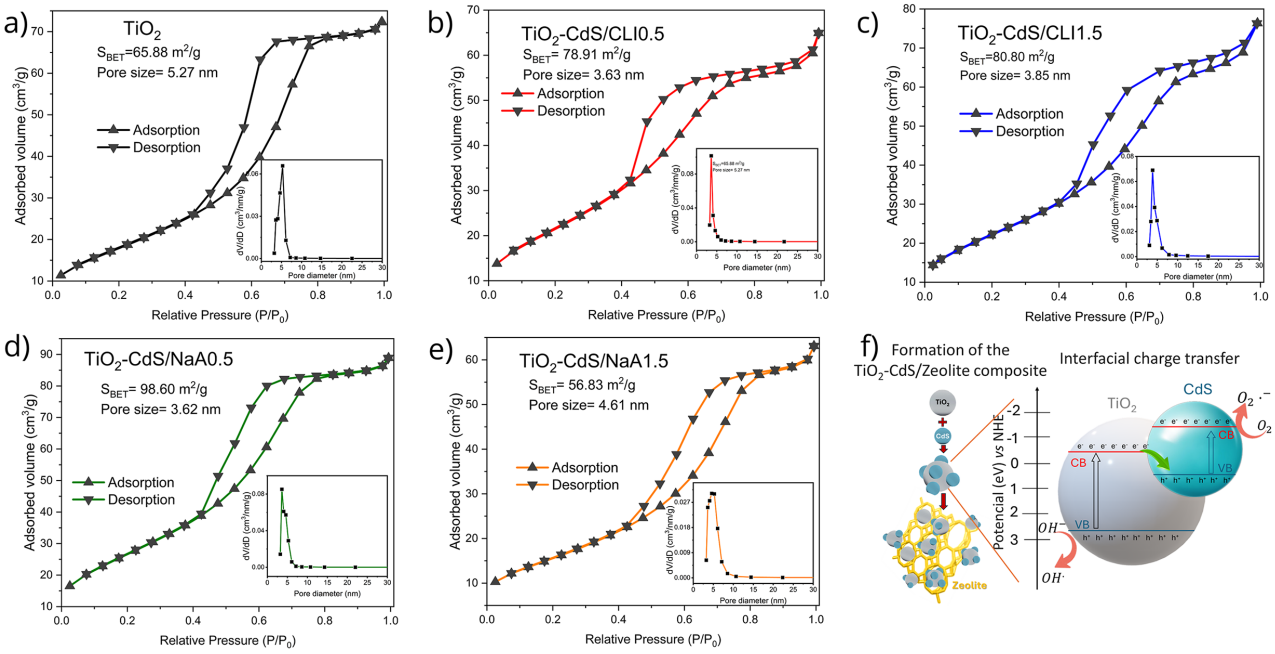

Fig. 5. Textural properties and the proposed charge-transfer mechanism. (a–e) N_2 adsorption-desorption isotherms. Inset: pore size distribution of TiO_2 particles and TiO_2-CdS/Zeolite composites. (f) TiO_2-CdS/Zeolite formation and proposed separation and charge transfer for the composite.

3.5 Photocatalytic Evaluation

The photocatalytic efficiency of the TiO_2-CdS/Zeolite composites was evaluated using MB (10 ppm) as a model molecule. 80 mL of the solution was used, and 24 mg of the catalyst was added. Prior to irradiation, the solution was placed in an ultrasonic bath in the dark for 30 min to reach adsorption-desorption equilibrium.

Photocatalytic degradation was carried out over 240 min using a fully reflective Sciencetech solar simulator with a 500 W xenon short-arc lamp. At 30-min intervals, an aliquot (approximately 5 mL) of the solution was taken and centrifuged to separate the particles and monitor changes in the absorbance intensity of the main MB band located at 665 nm. The Total Removal Efficiency was calculated using the following equation:

$$ED(\%) = \frac{C_0 - C_t}{C_0} * 100 = \frac{A_0 - A_t}{A_0} * 100. \quad (3)$$

Where C_0, A_0 correspond to the initial concentration and absorbance of the dye, respectively. C_t, A_t are the concentration and absorbance of the dye at time t, respectively.

Fig. 6a shows the absorbance spectra of MB, indicating that the intensity of the main band at 665 nm decreases with increasing irradiation time. Fig. 6b displays concentration versus time graphs, indicating that irradiation alone has a negligible effect on the dye. The TiO_2-CdS/CLI0.5 and TiO_2-CdS/CLI1.5 composites exhibit higher contaminant adsorption, at 16% and 54%, respectively, compared to TiO_2-CdS/NaA0.5 and TiO_2-CdS/NaA1.5, which reach only 4% and 8% (shaded area in Fig. 6b). This substantial difference in adsorption capacity is attributed to the ions present in the supports: clinoptilolite contains K^+, Mg^{2+}, and Ca^{2+} ions, which are more readily exchanged with MB molecules than the Na^+ ions in synthetic zeolite [43]. Additionally, NaA-type zeolite possesses smaller pores than clinoptilolite, which restricts the adsorption of contaminant molecules [13].

Due to the initial adsorption process, the starting concentration for each sample differs at the onset of irradiation. Total removal efficiencies for both phases are: TiO_2-CdS/CLI0.5, 69%; TiO_2-CdS/CLI1.5, 87%; TiO_2-CdS/NaA0.5, 43%; and TiO_2-CdS/NaA1.5, 40%. During the irradiation phase, the absolute photocatalytic degradation contributions, determined by subtracting Dark Adsorption % from Total Removal %, are 53%, 33%, 39%, and 32%, respectively.

The Langmuir-Hinshelwood (L-H) kinetic model was employed to estimate the kinetic constants for the photocatalytic degradation of MB. The following equation was utilized for this analysis:

$$-\ln\left(\frac{C_t}{C_0}\right) = kt \quad (4)$$

Here, k represents the first-order pseudo-rate constant. Fig. 6c presents plots of $-\ln(C_t/C_0)$ versus time for the photocatalysts during MB degradation. The linear fits used

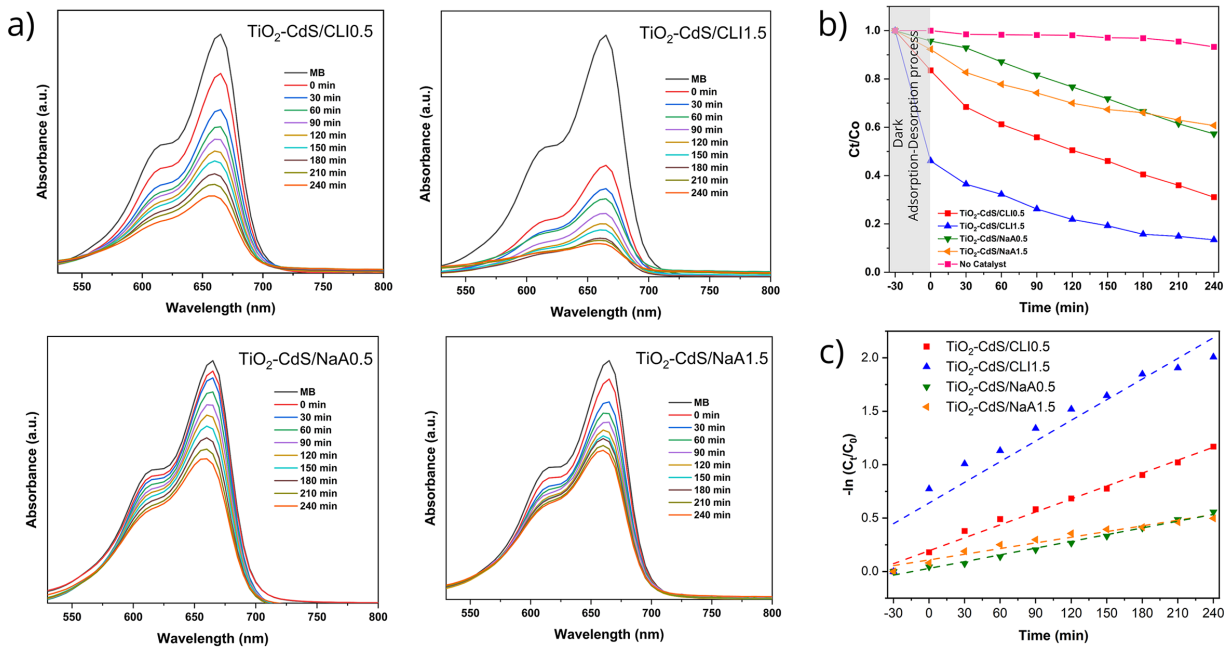

Fig. 6. Photocatalytic performance and degradation kinetics of methylene blue (MB). (a) Absorption spectra, (b) (C/C_0) versus time graphs for MB degradation recorded at different intervals during the photocatalytic test by the TiO_2-CdS/Zeolite composites and (c) degradation kinetics for MB by the composites.

Table 2. Summary of MB pollutant concentrations at the photocatalytic assessment stages.

Sample	Adsorption (Dark) (%)	Absolute Photocatalytic Degradation (%)			
		Ci (%)	Cf (%)	ED (%)	k (min^{-1})
TiO_2-CdS/CLI0.5	16	84	31	53	0.0042
TiO_2-CdS/CLI1.5	54	46	13	33	0.0051
TiO_2-CdS/NaA0.5	4	96	57	39	0.0022
TiO_2-CdS/ NaA1.5	8	92	60	32	0.0014

to determine k values (rate constants) demonstrated strong agreement with the data points (R^2 ≥0.98). Table 2 summarizes these results.

As summarized in Table 2, the TiO_2-CdS/CLI1.5 composite shows the highest apparent rate constant (k = 0.0051 min^{-1}), mainly due to its high initial dark adsorption (54%), which boosts dye concentration near the catalyst and speeds up degradation. However, the TiO_2-CdS/CLI0.5 composite (k = 0.0042 min^{-1}) remains the most balanced and efficient photocatalyst, achieving high degradation without relying primarily on physical adsorption from the zeolitic support.

In the photocatalytic process, the redox reactions responsible for degrading pollutant molecules occur at the photocatalyst's surface. Therefore, it is essential to ensure that the pollutant molecules are adsorbed onto the surface so that the photogenerated electron-hole pairs can perform their function. The following illustrates the possible mechanism for electron-hole pair generation and the photocatalytic degradation of MB using TiO_2-CdS/Zeolite composites.

Based on the structural properties and visible-light activity of the composites, a direct Z-scheme charge transfer mechanism is proposed. Under visible light irradiation, both TiO_2 (due to its sub-bandgap defect states) and CdS are excited, generating electron-hole pairs. In a typical Z-scheme heterojunction, the photogenerated electrons in the conduction band (CB) of TiO_2, which have a lower reduction potential, recombine directly with the holes in the valence band (VB) of CdS [44]. This efficient interfacial charge transfer significantly reduces bulk recombination within each semiconductor. Consequently, the highly reductive electrons in the CB of CdS remain available to reduce dissolved oxygen into superoxide radicals ($O_2 \cdot^-$) while the highly oxidative holes in the VB of TiO_2 oxidize water molecules into hydroxyl radicals ($OH \cdot$). These reactive oxygen species are ultimately responsible for the breakdown of the MB dye, as described by the following primary reaction steps [45,46]:

$$(\mathrm{Ti}O_2 - \mathrm{CdS/Zeolite}) + \mathrm{h}\nu \longrightarrow (\mathrm{Ti}O_2 - \mathrm{CdS/Zeolite}) + e^- + h^+ \quad (5)$$

$$(\mathrm{Ti}O_2 - \mathrm{CdS/Zeolite})\,(e^-) + O_2 \longrightarrow (\mathrm{Ti}O_2 - CdS/\mathrm{Zeolite}) + O_2{\cdot}^- \quad (6)$$

$$O_2\,{\cdot}^- + H_2O \longrightarrow HO_2 \cdot + OH^- \quad (7)$$

$$H_2O + (\mathrm{Ti}O_2 - CdS/\mathrm{Zeolite})\left(h^+\right) \longrightarrow H^+ + OH^{\cdot} \quad (8)$$

$$HO_2^- + H^+ \longrightarrow H_2O_2 \quad (9)$$

$$O_2\,{\cdot}^- + MB \longrightarrow CO_2 + H_2\mathrm{O} + \text{ Intermediate products} \quad (10)$$

$$OH^{\cdot} + \mathrm{MB} \longrightarrow CO_2 + H_2\mathrm{O} + \text{ Intermediate products} \quad (11)$$

$$h^+ + \mathrm{MB} \longrightarrow CO_2 + H_2\mathrm{O} + \text{ Intermediate products} \quad (12)$$

4. Discussion

For the photocatalytic process, the TiO_2-CdS/CLI0.5 composite exhibited the most balanced performance when considering both adsorption capacity and photocatalytic degradation efficiency. This behavior can be rationalized through a structure–property correlation analysis. The incorporation of clinoptilolite as a support promoted effective dispersion of TiO_2 crystallites, resulting in a reduced average crystallite size (~5.6 nm) without reaching the critical dimension (<5 nm) at which excessive surface defects may favor charge recombination [47,48,49].

Furthermore, Williamson-Hall analysis revealed moderate compressive lattice strain in this composite, suggesting interfacial structural distortion induced by CdS incorporation and potential interfacial interactions (such as electrostatic or partial Ti-O-Si linkages) with the zeolite framework. Such controlled lattice distortion can enhance charge separation by promoting internal electric fields at the heterojunction interface. This is consistent with the reduced photoluminescence intensity observed for the composite, indicating a decrease in electron-hole recombination.

In contrast, although the TiO_2-CdS/CLI1.5 sample exhibited higher adsorption due to increased zeolite content, the smaller crystallite size (<5 nm) may limit light absorption efficiency and increase surface defect density, negatively affecting charge carrier dynamics. Therefore, the superior photocatalytic response of TiO_2-CdS/CLI0.5 is attributed to different parameters such as crystallite size, moderate lattice strain, interfacial bonding, and reduced recombination rate, highlighting the importance of support and ionic composition in the performance of TiO_2–CdS/zeolite hybrid composites.

Limitations

While this study establishes the fundamental microstructural and optical properties of the TiO_2-CdS/Zeolite composites, certain limitations should be acknowledged. The photocatalytic evaluations were conducted as initial proof-of-concept tests using a single model pollutant (methylene blue) at a fixed concentration and a specific catalyst dosage. Exhaustive multi-batch reproducibility analyses, kinetic scavenger modeling for the absolute quantification of reactive oxygen species, and long-term stability/recyclability cycles were not performed at this fundamental stage. Future operational studies must address these engineering parameters to facilitate the transition of these materials toward scalable environmental remediation applications.

5. Conclusions

The development of TiO_2-CdS/Zeolite heterostructures demonstrates that Clinoptilolite and Zeolite A matrices function as rigid nanoreactors that restrict crystallite growth, prevent agglomeration, and induce a net compressive micro-strain through ionic radius mismatch. This microstructural distortion, along with the generation of deep trap states, such as oxygen and sulfur vacancies, extends optical absorption into the visible light spectrum. Furthermore, the synergistic integration of TiO_2 and CdS operates via a direct Z-scheme charge-transfer mechanism, which maximizes the system's redox potential by efficiently separating photogenerated electron-hole pairs and mitigating recombination.

In particular, the TiO_2-CdS/CLI0.5 system exhibited enhanced visible-light photocatalytic activity. While this study establishes the fundamental microstructural and optical properties of these ternary compounds, future research will focus on the exhaustive optimization of operational parameters, statistical reproducibility, long-term stability cycling, and mechanistic scavenger evaluations.

Availability of Data and Materials

The datasets used and analyzed during the current study are available from the corresponding author on reasonable request.

Author Contributions

HACH: Writing-original draft, conceptualization, methodology. ERM: Writing-review and editing, supervision, resources, and analyzed and interpreted the data and prepared the figures. LRB: Investigation, conceptualization, data curation, supervision, and resources. MGHC: Supervision, conceptualization, and characterization of the samples by XRD. FSD: Formal analysis, investigation, methodology, and participation in the analysis of the study samples. MCAC: Carried out the photocatalytic tests and data collection, formal Analysis, writing-Review, editing. All authors contributed to editorial changes in the manuscript. All authors read and approved the final manuscript. All authors have participated sufficiently in the work and agreed to be accountable for all aspects of the work.

Ethics Approval and Consent to Participate

Not applicable

Acknowledgment

Hugo Armando de la Cruz Hernández gratefully acknowledges the graduate fellowship from SECIHTI-México. The authors also thank the Laboratory of Nanotechnology for Applications in Biomedicine and the Environment (DAIA-UJAT) for supporting this work.

Funding

This research received no external funding.

Conflicts of Interest

The authors declare no conflicts of interest.

References

[1] Raizada P, Sudhaik A, Singh P. Photocatalytic water decontamination using graphene and ZnO coupled photocatalysts: A review. Materials Science for Energy Technologies. 2019; 2: 509–525. https://doi.org/10.1016/J.MSET.2019.04.007

[2] Afreen G, Shoeb M, Upadhyayula S. Effectiveness of reactive oxygen species generated from rGO/CdS QD heterostructure for photodegradation and disinfection of pollutants in waste water. Materials Science & Engineering. C, Materials for Biological Applications. 2020; 108: 110372. https://doi.org/10.1016/j.msec.2019.110372

[3] Uyen NN, Toan NC, Truong N, Tu LA, Le PH. Plasmonic Au-TiO_2 nanowire/nanotube heterostructures for multifunctional photocatalysis: dye and pesticide degradation, water splitting, and antibacterial activity. Nanoscale Advances. 2025; 7: 7317–7332. https://doi.org/10.1039/d5na00765h

[4] Vu VN, Thanh Pham TH, Le TH, Vuong TX. Enhanced removal of phenol red from water by Cu(ii)-modified Mg-Al composites *via* adsorption and photocatalysis. RSC Advances. 2025; 15: 28500–28523. https://doi.org/10.1039/d5ra02645h

[5] Kumari P, Kumar A. ADVANCED OXIDATION PROCESS: A remediation technique for organic and non-biodegradable pollutant. Results in Surfaces and Interfaces. 2023; 11: 100122. https://doi.org/10.1016/j.rsurfi.2023.100122

[6] Ma S, Wang W, Hu Z, Shi S, Yang P, Hou Y, et al. S-Scheme $CdS/CuWO_4$ Heterojunction Optimizes Reaction Kinetics for Enhanced Photocatalytic H_2 Evolution. Langmuir: the ACS Journal of Surfaces and Colloids. 2026; 42: 5156–5163. https://doi.org/10.1021/acs.langmuir.5c06431

[7] Xiang D, Chen C, Xie G, Gong Y, Ma J, Harkin-Jones E, et al. Mechanical property enhancement of basalt fiber-reinforced epoxy composites via construction of an organic/inorganic hybrid interface. Progress in Natural Science: Materials International. 2025; 35: 359–367. https://doi.org/10.1016/J.PNSC.2025.01.002

[8] Xu J, Lu Y, Zhao D, Du D, Song J. Synergistic enhancement of visible-light photocatalysis in X/Fe3O4/AlON heterojunctions for efficient and recoverable dye degradation. Ceramics International. 2026; 52: 2643–2653. https://doi.org/10.1016/J.CERAMINT.2025.12.081

[9] Manzoor S, Ashiq MF, Usman M, Sadaqat M, Mahmood K, Munawar T, et al. Development of excellent and novel flowery zirconia/cadmium sulfide nanohybrid electrode: For high performance electrochemical supercapacitor application. Journal of Energy Storage. 2021; 40: 102718. https://doi.org/10.1016/j.est.2021.102718

[10] Mohammed-Amine E, Kaltoum B, El Mountassir EM, Abdelaziz AT, Stephanie R, Stephanie L, et al. Novel sol-gel synthesis of TiO2/BiPO4 composite for enhanced photocatalytic degradation of carbamazepine under UV and visible light: Kinetic, identification of photoproducts and mechanistic insights. Journal of Water Process Engineering. 2025; 70: 107098. https://doi.org/10.1016/J.JWPE.2025.107098

[11] Sukhatskiy Y, Mnykh R, Tsymbaliuk V, Shepida M, Sozanskyi M, Znak Z. Ultrasound-assisted synthesis of Cu2O nanoparticles-clinoptilolite composites: Characterization, antifungal activity, and effectiveness in sonocatalytic periodate activation for oxidative degradation of acid red 14 dye. Journal of Water Process Engineering. 2025; 74: 107792. https://doi.org/10.1016/J.JWPE.2025.107792

[12] Huang Z, Su JF, Guo YH, Su XQ, Teng LJ. Synthesis of well-crystallized zeolite beta at large scale and its incorporation into polysulfone matrix for gas separation. Chemical Engineering Communications. 2009; 196: 969–986.

[13] de Dios FS, Morales ER, Del Carmen Arellano Cortaza M, Hernández GP, Mandujano EVM, Alejandro EML, et al. Improvement of photocatalysis using ZnO/zeolite nanocomposites for contaminant removal in aqueous media. Desalination and Water Treatment. 2023; 312: 79–88. https://doi.org/10.5004/DWT.2023.29961

[14] Hossain MS, Ahmed S. Easy and green synthesis of TiO2 (Anatase and Rutile): Estimation of crystallite size using Scherrer equation, Williamson-Hall plot, Monshi-Scherrer Model, size-strain plot, Halder- Wagner Model. Results in Materials. 2023; 20: 100492. https://doi.org/10.1016/J.RINMA.2023.100492

[15] Mote VD, Purushotham Y, Dole BN. Williamson-Hall analysis in estimation of lattice strain in nanometer-sized ZnO particles. Journal of Theoretical and Applied Physics. 2023; 6. https://doi.org/10.1186/2251-7235-6-6

[16] Piler K, Bahrim C, Twagirayezu S, Benson TJ. Lattice disorders of TiO2 and their significance in the photocatalytic conversion of CO2. Advances in Catalysis (vol. 66, pp. 109–233). Elsevier: place. 2020.

[17] Moghaddam HM, Nasirian S. Dependence of activation energy and lattice strain on TiO 2 nanoparticles? Nanoscience Methods. 2012; 1: 201–212. https://doi.org/10.1080/17458080.2011.620023

[18] Hu Y, Pan Y, Wang Z, Lin T, Gao Y, Luo B, et al. Lattice distortion induced internal electric field in TiO_2 photoelectrode for ef-

ficient charge separation and transfer. Nature Communications. 2020; 11: 2129. https://doi.org/10.1038/s41467-020-15993-4
[19] Hakki A, Yang L, Wang F, Macphee DE. The Effect of Interfacial Chemical Bonding in TiO2-SiO2 Composites on Their Photocatalytic NOx Abatement Performance. Journal of Visualized Experiments: JoVE. 2017; 56070. https://doi.org/10.3791/56070
[20] Gholizadeh A. The effects of A/B-site substitution on structural, redox and catalytic properties of lanthanum ferrite nanoparticles. Journal of Materials Research and Technology. 2019; 8: 457–466. https://doi.org/10.1016/J.JMRT.2017.12.006
[21] Chai Y, Dai W, Wu G, Guan N, Li L. Confinement in a Zeolite and Zeolite Catalysis. Accounts of Chemical Research. 2021; 54: 2894–2904. https://doi.org/10.1021/acs.accounts.1c00274
[22] Jalloul G, Al-Mousawi A, Chocr F, Merhi A, Awala H, Boyadjian C. Fe-sensitized zeolite supported TiO2 for the degradation of tetracycline using blue LED irradiation. Frontiers in Environmental Science. 2022; 10: 873257. https://doi.org/10.3389/fenvs.2022.873257
[23] Bukit N, Ginting EM, Frida E, Bukit BF. Physical analysis of TiO2 and bentonite nanocomposite as adsorbent materials. Reviews on Advanced Materials Science. 2021; 60: 912–920. https://doi.org/10.1515/rams-2021-0076
[24] Lafjah M, Djafri F, Bengueddach A, Keller N, Keller V. Beta zeolite supported sol-gel TiO2 materials for gas phase photocatalytic applications. Journal of Hazardous Materials. 2011; 186: 1218–1225. https://doi.org/10.1016/j.jhazmat.2010.11.134
[25] Celeste A, Agostini M, De Bonis A, Brutti S. Insight the lithiation process of Micro and Nanoparticles TiO2-Anatase based electrodes. Electrochimica Acta. 2025; 535: 146618. https://doi.org/10.1016/J.ELECTACTA.2025.146618
[26] Castrejón-Sánchez VH, Camps E, Camacho-López M. Quantification of phase content in TiO2 thin films by Raman spectroscopy. Superficies y Vacío. 2014; 27: 88–92.
[27] Khalyavka TO, Shymanovska VV, Gavrilko TA, Manuilov EV, Klishevich GV, Szymański D, et al. Synthesis and characterization of nanostructured Co-Si co-doped TiO2 with enhanced visible-light photocatalytic performance in phenol red degradation. Ceramics International. 2026; 52: 1221–1236. https://doi.org/10.1016/J.CERAMINT.2025.11.432
[28] El Bendali A, Aqil M, Hdidou L, El Halya N, El Ouardi K, Alami J, et al. The Electrochemical and Structural Changes of Phosphorus-Doped TiO_2 through In Situ Raman and In Situ X-Ray Diffraction Analysis. ACS Omega. 2024; 9: 14911–14922. https://doi.org/10.1021/acsomega.3c08122
[29] Zhang W, Xiao X, Zheng L, Wan C. Fabrication of TiO2/MoS2@zeolite photocatalyst and its photocatalytic activity for degradation of methyl orange under visible light. Applied Surface Science. 2015; 358: 468–478. https://doi.org/10.1016/J.APSUSC.2015.08.054
[30] Awada C, Kanoun MB, Ahmed F, Saber O, Osama A, Osama M, et al. Size effect in plasmonic-enhanced photocatalysis in Au/TiO2 nanocomposites. Optical Materials. 2025; 167: 117293. https://doi.org/10.1016/J.OPTMAT.2025.117293
[31] Justel T, Wiechert DU, Lau C, Sendor D, Kynast U. Optically functional zeolites: Evaluation of UV and VUV stimulated photoluminescence properties of Ce super (3+)- and Tb super (3+)-doped zeolite X. Advanced Functional Materials. 2001; 11: 105–110. https://doi.org/10.1002/1616-3028(200104)11:2%3C105::AID-ADFM105%3E3.0.CO;2-J
[32] Milani M, Magnacca G, Valsania MC, Marchini E, Molinari A. A physico-chemical insight into the benzaldehyde reduction mechanism catalysed by CdS/TiO2 composites activated by visible light. Results in Chemistry. 2026; 19: 102914. https://doi.org/10.1016/J.RECHEM.2025.102914
[33] Duan J, Zhao Y, Wu Y, Liu Y, Chen J, Yang R, et al. Strain-induced charge delocalization achieves ultralow exciton binding energy toward efficient photocatalysis. Chemical Science. 2024; 15: 19546–19555. https://doi.org/10.1039/d4sc05873a
[34] Mascaretti L, Russo V, Zoppellaro G, Lucotti A, Casari CS, Kment Š, et al. Excitation Wavelength- and Medium-Dependent Photoluminescence of Reduced Nanostructured TiO2 Films. The Journal of Physical Chemistry C. 2019; 123: 11292–11303. https://doi.org/10.1021/acs.jpcc.9b01727
[35] Pallotti DK, Passoni L, Maddalena P, Di Fonzo F, Lettieri S. Photoluminescence Mechanisms in Anatase and Rutile TiO2. The Journal of Physical Chemistry C. 2017; 121: 9011–9021. https://doi.org/10.1021/acs.jpcc.7b00321
[36] Brüninghoff R, Wenderich K, Korterik JP, Mei BT, Mul G, Huijser A. Time-dependent photoluminescence of nanostructured anatase TiO2 and the role of bulk and surface processes. The Journal of Physical Chemistry C. 2019; 123: 26653–26661.
[37] Bedrouni M, Bennabi F, Farah BL, Ameri I, Guezzoul M. Defect-engineered Tb/In co-doped anatase TiO2 thin films with enhanced antimicrobial activity and tailored electronic structure. Physica B: Condensed Matter. 2026; 723: 418064. https://doi.org/10.1016/j.physb.2025.418064
[38] Rostas AM, Suciu RC, Roşu MC, Turza A, Cosma DV, Tripon S, et al. Annealing temperature, a key factor in shaping Ag-decorated TiO2 aerogels as efficient visible-light photocatalysts. Mater Chem Phys. 2025; 337: 130557. https://doi.org/10.1016/j.matchemphys.2025.130557
[39] Hamid K, Bin Mukhlish MZ, Uddin MT. Sunlight-activated heterostructure MoS_2/CdS nanocomposite photocatalyst with enhanced photocatalytic activity: band alignment and mechanism study. RSC Advances. 2024; 14: 38908–38923. https://doi.org/10.1039/d4ra06857b
[40] Dhage SR, Colorado HA, Hahn HT. Photoluminescence properties of thermally stable highly crystalline CdS nanoparticles. Materials Research. 2013; 16: 504–507. https://doi.org/10.1590/S1516-14392013005000020
[41] Muttakin M, Mitra S, Thu K, Ito K, Saha BB. Theoretical framework to evaluate minimum desorption temperature for IUPAC classified adsorption isotherms. International Journal of Heat and Mass Transfer. 2018; 122: 795–805. https://doi.org/10.1016/j.ijheatmasstransfer.2018.01.107
[42] Lee S, Park Y, Choi M. Cooperative interplay of micropores/mesopores of hierarchical zeolite in chemical production. ACS Catalysis. 2024; 14: 2031–2048. https://doi.org/10.1021/acscatal.3c05170
[43] Tubon-Usca G, Centeno C, Pomasqui S, Beneduci A, Arias FA. Enhanced adsorption of methylene blue in wastewater using natural zeolite impregnated with graphene oxide. Applied Sciences. 2025; 15: 2824. https://doi.org/10.3390/app15052824
[44] Ighnih H, Ouachtak H, Jada A, Ait Addi A. Construction of BiOBr/g-C3N4/Kaolinite Z-scheme heterojunction photocatalysts for highly efficient photocatalytic degradation of organic pollutants. Materials Science in Semiconductor Processing. 2026; 207: 110478. https://doi.org/10.1016/J.MSSP.2026.110478
[45] Sher M, Javed M, Shahid S, Iqbal S, Qamar MA, Bahadur A, et al. The controlled synthesis of g-C_3N_4/Cd-doped ZnO nanocomposites as potential photocatalysts for the disinfection and degradation of organic pollutants under visible light irradiation. RSC Advances. 2021; 11: 2025–2039. https://doi.org/10.1039/d0ra08573a
[46] Qamar MA, Shahid S, Javed M, Sher M, Iqbal S, Bahadur A, et al. Fabricated novel g-C3N4/Mn doped ZnO nanocomposite as highly active photocatalyst for the disinfection of pathogens and degradation of the organic pollutants from wastewater under sunlight radiations. Colloids and Surfaces A: Physicochemical and Engineering Aspects. 2021; 611: 125863. https://doi.org/

10.1016/J.COLSURFA.2020.125863
[47] Lee S, Cho I, Noh J, Hong KS, Han GS, Jung HS, et al. Correlation of anatase particle size with photocatalytic properties. Physica Status Solidi (a). 2010; 207: 2288–2291. https://doi.org/10.1002/pssa.200925504
[48] Amano F, Ishinaga E, Yamakata A. Effect of particle size on the photocatalytic activity of WO3 particles for water oxidation. The Journal of Physical Chemistry C. 2013; 117: 22584–22590. https://doi.org/10.1021/jp408446u
[49] Wang X, Sø L, Su R, Wendt S, Hald P, Mamakhel A, et al. The influence of crystallite size and crystallinity of anatase nanoparticles on the photo-degradation of phenol. Journal of Catalysis. 2014; 310: 100–108. https://doi.org/10.1016/j.jcat.2013.04.022